# Morphodynamics of Fluid-Fluid Displacement in Three-Dimensional Deformable Granular Media

Marie-Julie Dalbe[†] and Ruben Juanes[*]
*Massachusetts Institute of Technology, 77 Massachusetts Avenue, Cambridge, Massachusetts 02139, USA*

(Received 23 August 2017; revised manuscript received 23 January 2018; published 26 February 2018)

We study experimentally the displacement of one fluid by another in a granular pack to uncover relationships between fluid invasion and medium deformation. We develop an experimental setup that allows us to reconstruct the coupled invasion-deformation dynamics in 3D. We simultaneously characterize the fluid invasion pattern and document a transition from fluid-fluid displacement in pores to the formation of conduits by grain motion. We rationalize the findings in terms of a simple poromechanics model that indeed captures this transition as a result of the balance between viscous and frictional forces. These results contribute to elucidating the role of three dimensionality in the timing, mode, and morphology of fluid-fluid displacement and injection-induced deformation in porous media.

DOI: 10.1103/PhysRevApplied.9.024028

## I. INTRODUCTION

Multiphase flow in porous media plays a fundamental role in many natural and engineered processes, including enhanced oil recovery [1,2], geothermal energy production [3], geologic $CO_2$ sequestration [4,5], water infiltration in soil [6,7], and water dropout in fuel cells [8], to name just a few. Of particular complexity and importance are processes that involve the simultaneous displacement of fluids and deformation of the host medium, with applications as varied as shale-oil and shale-gas production via hydraulic fracturing [9,10], methane venting from organic-rich sediments [11], hydrate formation and dissociation [12–14], volcanic eruptions [15], desiccation cracks in soil [16], air sparging for subsurface contaminant remediation [17,18], and patterning of carbon-nanotube forests [19].

Studies investigating the morphology of the deformation of granular packs from fluid injection have almost exclusively been conducted in quasi-2D experimental setups. For single-phase fluid flows, early experiments demonstrated a transition from viscous fingering to fracturing in clay slurries [20,21], and recent work has shown the emergence of inelastic deformation from the collective rearrangement of a 2D monolayer of elastic frictionless hydrogel particles [22]. Fracture patterns have also been observed in loose and dense systems such as particle rafts as a result of surfactant spreading [23,24], and colloidal suspensions as a result of drying [25,26]. Two-phase flow experiments of air injection into liquid-filled granular packs have elucidated a transition from Saffman-Taylor–type fingering to fracturing as the packing ratio increases [27]. This type of fluid-fluid-particle displacement of a granular suspension can lead to a variety of fascinating invasion patterns, including labyrinth structures [28], coral morphologies, and stick-slip bubbles [29].

Of particular interest to us are systems at high packing density which display a transition from pore-scale fingering to hydrocapillary fracturing, as a result of the interplay between viscous and capillary forces and frictional forces [30–32]. This balance of forces at the pore scale permits rationalizing observations in a wide range of systems, including gas injection into water-saturated granular packs [33–36] and clays [37], liquid imbibition into sand [38], desiccation cracks [39], $CO_2$ migration in porous rocks [40], and methane venting from soft sediments [11,41,42].

Three-dimensional visualizations of multiphase flow in porous media under dynamic conditions have relied on direct optical visualization [43], planar laser-fluorescence imaging similar to that we employ here [44–47], confocal microscopy [48], magnetic resonance imaging [49], and high-energy x-ray computed tomography [50,51]. While these 3D observations have been instrumental in characterizing fluid-fluid displacements—including temporally resolved imaging of pore-scale invasion events [50,51]—they have been limited to small sampling volumes and to rigid porous media that have left medium deformation unexplored.

Here, we perform 3D imaging of two-phase flow in a deformable porous medium, with an emphasis in understanding the morphology and dynamics of fluid invasion and medium deformation. We construct a porous cell made of borosilicate glass beads initially filled with glycerol to achieve refractive-index matching, and we inject a less viscous silicon oil that is also index matched. We employ a

---

[*] juanes@mit.edu

[†] Present address: Aix-Marseille Université, 49 Rue Joliot Curie, 13013 Marseille, France.

planar laser-fluorescence imaging technique in which a laser sheet mounted on a moving stage shines on the medium and excites fluorescent dyes premixed with the defending and invading fluids. To control the deformability of the medium, we apply a confining weight to the top lid of the cell. To elucidate the morphology of fluid invasion under different confining weights, bead sizes, and injection rates, we perform two different types of measurements and analyses:

1. Macroscopic (cell scale), in which we track the displacement of the top lid. We develop a coupled poromechanics model for the onset of frictional failure and the evolution of postfailure overall cell deformation, as a balance between fluid-fluid displacement and cavity expansion. Our model allows us to identify the relevant poromechanical parameters for our model system across a wide range of experimental conditions.
2. Microscopic (pore scale), in which time-lapse 3D imaging allows us to reconstruct in detail the morphology of the invading fluid and the bead-pack displacement. This analysis allows us to delineate the experimental conditions under which fluid invasion into the granular pack is controlled by either pore-scale fingering or conduit opening.

## II. LABORATORY EXPERIMENTS

### A. Experimental setup

We built a porous-medium cell consisting of an acrylic box (horizontal dimensions $L \times L$). The box, initially open at the top, is filled with borosilicate glass beads (nominal diameter, $d$), and a lid is placed at the top of the bead pack (initial height, $H_0$). This lid is drilled with holes (hole diameter, 1 mm), so as to allow uniform seepage of fluid through it while retaining the beads. A weight $W$ is placed on top of the lid to control the confining stress that the bead pack is subject to. The cell has a hole drilled at the center of the bottom face to allow the injection of fluid. A needle (internal diameter, 1.7 mm) is glued to the inside of this hole, and fluids are injected using a syringe pump (PHD 2000, Harvard Apparatus).

Initially, we pour the beads inside the container and place the lid on top, and then the confining weight. The dry bead pack is then filled with the initial defending fluid, glycerol, at a rate of 1 $\mathrm{ml\,min^{-1}}$. Glycerol is wetting to the glass beads with respect to air. Thus, injection of glycerol is a viscously stable, gravity-stable, slow imbibition that results in a complete displacement of air from the porous medium. The absence of air bubbles is checked optically. We stop injection once the glycerol has reached the top of the lid. We then inject the invading liquid at a rate $q$.

We employ cells of different dimensions ($L = \{2, 6\}$ cm, $H_0 = \{2.5, 4.5\}$ cm), beads of different diameters ($d = \{1, 3\}$ mm), and a range of values for the other control parameters ($0.045 < W < 23.9$ N, $0.03 < q < 100\,\mathrm{ml\,min^{-1}}$) to study fluid-fluid displacement under diverse experimental conditions.

### B. Imaging

We perform two types of experiments, according to the kind of imaging that is conducted: (1) direct imaging, and (2) planar laser-induced fluorescence (PLIF) imaging. In each type of experiment, we employ slightly different fluids—with, therefore, slightly different properties, which we describe next.

#### *1. Direct imaging*

In this set of experiments, we image the porous cell from one side using a digital CMOS camera (Hamamatsu ORCA-Flash4.0). The defending fluid, glycerol, has the same refraction index as borosilicate glass ($r = 1.430$), thereby rendering the porous medium transparent. The invading fluid is silicone oil (Sigma Aldrich), dyed with a blue dye (Orcosolve Oil Blue AP), and direct imaging records a 2D projection of the 3D fluid invasion pattern (Fig. 1). The properties of the fluids are given in Table I.

#### *2. PLIF imaging*

In a second set of experiments, we use the PLIF technique, which allows us to see through a transparent porous medium [44,46,47]. In this case, the invading fluid is also index matched to the borosilicate glass beads. We use a silicone oil that is a mix of two different products: 60.9% Dow Corning 556 and 39.1% Dow Corning 550. The proportions are determined experimentally so that the refractive index of the mix is as close as possible to that of the beads.

A laser sheet is used to illuminate a vertical plane of the bead pack (Z-Laser ZM18, emitting at 532 nm). Both the defending and invading liquids are dyed using different fluorescent dyes that are excited by the wavelength of the laser. The defending fluid (glycerol) is seeded with

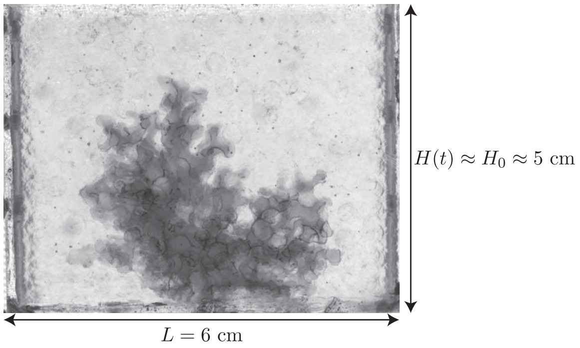

FIG. 1. Image taken by the camera during a direct-imaging experiment in a cell with horizontal dimension $L = 6$ cm and beads of diameter $d = 3$ mm. The dark pattern is the injected silicone oil.

TABLE I. Fluid properties for both types of experiments: density $\rho$, dynamic viscosity $\eta$, viscosity contrast $M$, and interfacial tension $\gamma$.

| | Direct imaging | | PLIF imaging | |
|---|---|---|---|---|
| Defending fluid | Glycerol | $\rho_d = 1260\ \mathrm{kg\,m^{-3}}$<br>$\eta_d = 1410\ \mathrm{mPa\,s}$ | Glycerol with Rhodamine 590 Chloride | $\rho_d = 1260\ \mathrm{kg\,m^{-3}}$<br>$\eta_d = 1410\ \mathrm{mPa\,s}$ |
| Invading fluid | Silicon oil with Orcosolve Blue | $\rho_i = 960\ \mathrm{kg\,m^{-3}}$<br>$\eta_i = 48\ \mathrm{mPa\,s}$ | Dow Corning mix with Pyrromethene 567A | $\rho_i = 1013\ \mathrm{kg\,m^{-3}}$<br>$\eta_i = 53\ \mathrm{mPa\,s}$ |
| Fluid-pair interaction | | $M = 29$<br>$\gamma = 26\ \mathrm{mN\,m^{-1}}$ | | $M = 27$<br>$\gamma = 19\ \mathrm{mN\,m^{-1}}$ |

Rhodamine 590 Chloride (Exciton) at a concentration of $0.12\ \mathrm{mg\,l^{-1}}$. The invading fluid (silicone oil) is seeded with Pyrromethene 567A (Exciton) at a concentration of $2.7\ \mathrm{mg\,l^{-1}}$. The fluid properties are given in Table I. The two dyes emit at a similar wavelength, around 560 nm. We place a long-pass filter, keeping light with a wavelength longer than 550 nm only, ensuring that the light emitted directly by the laser does not reach the camera. We use different dye concentrations so that, in the illuminated plane, we can distinguish the beads and the two fluids: the beads appear black, the defending fluid gray, and the invading fluid white. The laser and the camera are mounted on a motorized stage to scan the entire porous cell and obtain a 3D reconstruction of the dynamics of invasion (Fig. 2). Images are taken at $1024 \times 1024$ pixels, giving a resolution of 80–100 $\mu$m/pixel. The maximum width of the laser sheet is 0.3 mm, which is well below one bead diameter. Thus, individual pore volumes are lit during a given scan, and we believe that the measurements would not be different if the laser sheet width were smaller. The frequency of images is such that the separation between planes is 0.5 mm for the large cell ($L = 6$ cm) and 0.2 mm for the small cell ($L = 2$ cm). The time lapse between 3D-imaging cycles of the cell is 4.0 s for the large cell, and 4.5 s for the small cell.

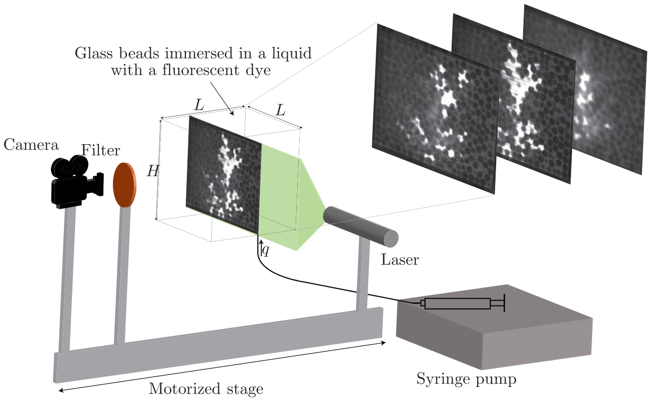

FIG. 2. Schematic of the experimental setup for PLIF imaging. The cubic cell is filled with borosilicate glass beads. We first inject glycerol, which is the defending fluid. Then we inject a mix of Dow Corning silicone oil at a constant injection rate $q$ with a syringe pump. We shine a laser sheet through the cell that excites the defending and invading fluids, and we image using a camera filtering out the light emitted directly by the laser. The beads appear black, the defending fluid gray, and the invading fluid white. The laser and the camera are mounted on a motorized stage, which allows scanning of the entire cell.

### C. Wetting properties

We employ borosilicate glass beads (Corning 7268 from Sigma Aldrich for the 3-mm beads, CG-1101 from Chemglass for the 1-mm beads), which we reuse from one experiment to the next. We ensure reproducibility of the wetting properties of the beads by following a six-step cleaning process before each experiment: (1) wash with acetone to remove most of the silicone oil; (2) wash with isopropanol to dilute the glycerol, let soak overnight; (3) wash with a solvent remover, soap, and water; (4) let dry on a hot plate at 75 °C for 12 h; (5) wash with a piranha solution (mix of 75% hydrogen peroxide and 25% sulfuric acid); and (6) let dry in the oven at 75 °C for 24 h. Following this cleaning procedure, the beads are exposed to a handheld plasma for 10 min or to an ozone cleaner in order to alter their wetting properties.

We measure the contact angle between the two fluids directly on the glass beads using a goniometer (ramé hart, Model 590). The contact angle is the same, within the measurement uncertainty, for the two pairs of fluids (glycerol–silicone oil and glycerol–Dow Corning mixes). Experimentally, we immerse a glass bead into silicone oil, deposit a droplet of glycerol on top of it, and then measure the static contact angle. The contact angle through the dense glycerol phase is $\theta = 35 \pm 8°$ (Fig. 3).

Therefore, our fluid-fluid displacement experiments are in the drainage, unfavorable-mobility regime: a less wetting,

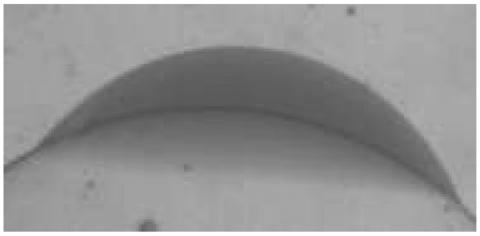

FIG. 3. Image from the goniometer during measurement of the contact angle. We deposit a droplet of glycerol (dark gray) on a glass bead immersed in silicone oil.

less viscous fluid (oil) displacing a more wetting, more viscous fluid (glycerol).

### D. Bead-pack properties

We determine the flow properties of the glass-bead pack: porosity and permeability. We determine porosity by weighting the cell before and after filling it with glycerol, a fluid of known density. The porosity determined in this way is $\phi_0 = 0.48 \pm 0.02$ for both bead diameters used ($d = 1$ and 3 mm).

We measure the intrinsic permeability $k_0$ of the bead pack using the constant-head method [52]. We use a rectangular cell with a sieve at the bottom so that the beads stay in the cell, while the liquid can escape. We use a syringe pump to keep the level of liquid at the top of the cell constant. The cell is put inside a container with a fixed level of liquid, which can overflow in a larger container, and we measure the rate of liquid overflowing.

For the 3-mm beads, the liquid used is glycerol. We measure $k_0/\eta = 9.5 \pm 0.2 \times 10^{-9}\ \mathrm{m\,s\,kg^{-1}}$. Taking the dynamic viscosity $\eta = 1.41$ Pa s, we obtain $k_0 = 1.3 \times 10^{-8}\ \mathrm{m}^2$. For the 1-mm beads, the liquid used is a mixture of water and glycerol of viscosity $\eta = 0.143$ Pa s, and we measure $k_0 = 1.3 \times 10^{-9}\ \mathrm{m}^2$.

We can compare this value with the one given by the Kozeny-Carman equation [52]:

$$k_{\mathrm{KC}} = \frac{d^2}{180} \frac{\phi_0^3}{(1-\phi_0)^2}, \tag{1}$$

which gives $k_{\mathrm{KC}} = 2.0 \times 10^{-8}\ \mathrm{m}^2$ for $d = 3$ mm, and $k_{\mathrm{KC}} = 2.3 \times 10^{-9}\ \mathrm{m}^2$ for $d = 1$ mm—a discrepancy of about 40% with respect to the experimental values that can easily be attributed to the lack of monodispersity of the granular pack.

## III. POROMECHANICS MODEL

Fluid injection into the fluid-filled granular cell pressurizes the fluid in the cell, which has two main effects: (1) fluid invasion and displacement of the immiscible defending fluid, and (2) deformation of the granular pack. These two effects are interdependent, and this coupling is generally known as *poromechanics* [53–56].

Here, we develop a simplified poromechanics model that will allow us to rationalize the behavior observed in the experiments, which is reported on in Sec. IV. In simple terms, the behavior is as follows: the granular pack experiences small deformations initially, behaving elastically, up to a point at which a cavity near the injection port forms, displacing the grains and opening a conduit that is observable macroscopically. Fundamentally, we are interested in characterizing and predicting the onset of fluid-driven granular failure, and the macroscopic evolution of deformation after failure.

In what follows, we develop this model, staging the development into prefailure, the onset of failure, and postfailure.

### A. Poroelastic model before frictional failure

Before the granular pack experiences large irreversible deformations, the evolution of pore pressure and skeleton deformation can be described by the field theory of poroelasticity in small deformations [53–56]. The equation for the evolution of pore pressure $p$ takes the form

$$\left(\frac{b^2}{K_d} + \frac{1}{M}\right)\frac{\partial p}{\partial t} + \frac{b}{K_d}\frac{\partial \sigma_V}{\partial t} + \boldsymbol{\nabla} \cdot \mathbf{v} = 0, \tag{2}$$

where $K_d$ is the dry bulk modulus, $b$ is the Biot coefficient, $M$ is the Biot modulus, $\sigma_V$ is the volumetric stress, and $\mathbf{v}$ is the seepage velocity of the fluid with respect to the solid. For incompressible fluids and grains (that is, when all the deformation can be attributed to grain rearrangement), $M \to \infty$ and $b \to 1$, and we can define the piezometric head as $h = p/(\rho_f g)$, where $\rho_f$ is the fluid density and $g$ is the gravitational acceleration.

If we assume constant load conditions, $\sigma_V \approx$ const and, using Darcy's law for the seepage velocity,

$$\mathbf{v} = -K \boldsymbol{\nabla} h, \tag{3}$$

where $K = k\rho_f g/\eta_f$ is the hydraulic conductivity. Defining the hydraulic diffusivity, $D = (k/\eta)K_d = K/(\rho_f g)K_d$, the poroelastic pressure equation reduces to

$$\frac{\partial h}{\partial t} - D\boldsymbol{\nabla}^2 h = 0, \tag{4}$$

which, under these assumptions, is decoupled from the linear momentum balance governing medium deformation.

This canonical diffusion equation has been solved under many different geometries and boundary conditions (see, e.g., Refs. [55,57,58]). Here, we put forward a simplified configuration that reasonably represents the flow in our porous cell.

Given the point injection, the cubiclike dimensions of the cell, and the uniform seepage through the top boundary, we assimilate the physical problem to a pressure-diffusion problem on a hollow half sphere (outer radius $R$ and inner radius $a$) under radial symmetry, with a prescribed flow rate $q$ at the inner boundary, and a constant piezometric head equal to the initial piezometric head (taken as a reference, $h = 0$) at the outer boundary. We have confirmed, via 3D finite-element simulations of Eq. (4) with the appropriate boundary conditions, that the behavior of the solutions in the actual box geometry and the half-sphere geometry are very close to each other (within 5% for radial distances $r < 10$ mm), thereby justifying the adoption of the half-sphere geometry as a valid approximation for our purposes.

Mathematically, the initial and boundary value problem (IBVP) takes the form

$$\frac{\partial h}{\partial t} = \frac{1}{r^2}\frac{\partial}{\partial r}\left(Dr^2\frac{\partial h}{\partial r}\right), \qquad a < r < R, \qquad t > 0, \tag{5}$$

$$h(r,0) = 0, \qquad a < r < R, \tag{6}$$

$$h(R,t) = 0, \qquad t > 0, \tag{7}$$

$$4\pi a^2 K \frac{\partial h}{\partial r}\bigg|_{r=a} = -2q, \qquad t > 0. \tag{8}$$

The solution to this IBVP can be obtained via the change of variable $u := hr$ and using the method of separation of variables [59]:

$$h(r,t) = \frac{2q}{4\pi K}\frac{1}{r}\cdot\left[\left(1-\frac{r}{R}\right) - 2\sum_{n=1}^{\infty}\frac{1}{1+\frac{R-a}{a}(1+a^2\lambda_n^2)} \times \frac{\sin[\lambda_n(R-r)]}{\sin[\lambda_n(R-a)]}\exp(-D\lambda_n^2 t)\right], \tag{9}$$

where the eigenvalues $\lambda_n$ satisfy the nonlinear equation

$$\tan[\lambda_n(R-a)] + a\lambda_n = 0, \qquad n = 1, 2, \ldots. \tag{10}$$

For illustration, we plot the solution as a function of radial distance $r$ at different times for parameters corresponding to the large cell ($R = 4.5$ cm) filled with the large beads ($d = 3$ mm) and an effective dry bulk modulus $K_d = 10$ kPa. The solution $h(r,t)$ exhibits a fast transient reaching steady state within approximately 10 s (Fig. 4, top panel). By plotting the time derivative $\dot{h}(r,t)$, we observe a pressure pulse that propagates from the injection point ($r = a$) outwards (Fig. 4, bottom panel).

### B. Onset of frictional failure

We estimate, based on simple considerations of frictional failure, the critical value of the piezometric head change, $h_f$, that will lead to particle rearrangement within the granular pack. We assume that the initial stress state of the granular pack is controlled by the confining weight on top of the lid, the weight of the beads and the interstitial fluid, and the lateral confinement provided by the vertical walls of the cubic pack. Thus, the total vertical stress is geostatic, $\sigma_v = (W/L^2) + \rho_b g z$, the pore pressure is hydrostatic, $p = \rho_f g z$, and, therefore, the vertical and horizontal effective stresses at the bottom of the cell are

$$\sigma'_v = \frac{W}{L^2} + \rho' g H_0, \tag{11}$$

$$\sigma'_h = K_0 \sigma'_v, \tag{12}$$

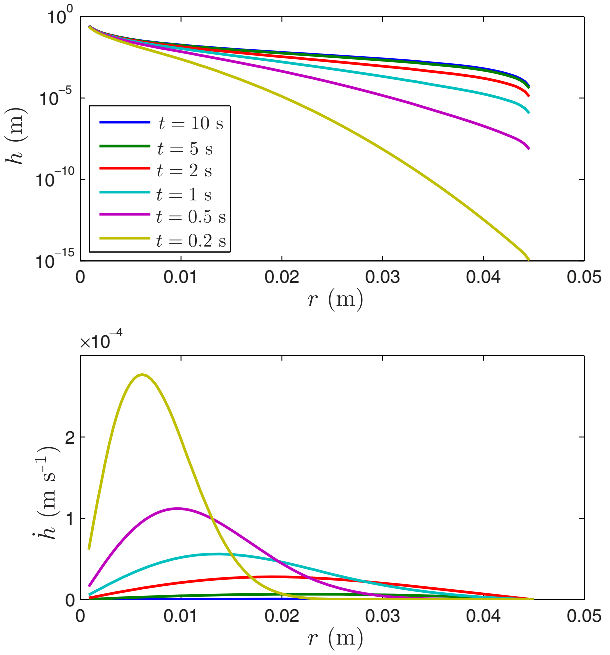

FIG. 4. Behavior of the solution [Eq. (9)] to the poroelastic diffusion IBVP [Eqs. (5)–(8)]. (Top panel) Piezometric head $h(r,t)$. (Bottom panel) Time derivative $\dot{h}(r,t)$. See the text for details on the parameters used.

where $\rho' = \rho_b - \rho_f$ is the buoyant density, and $K_0$ is the coefficient of lateral stress at rest.

We employ the Mohr-Coulomb failure criterion for cohesionless granular materials:

$$\tau = \mu_f \sigma'_n, \tag{13}$$

where $\tau$ is the shear stress, $\sigma'_n$ is the normal effective stress, and $\mu_f$ is the coefficient of friction. Using the common Mohr-circle interpretation, failure is attained once the pressure is increased sufficiently to move the Mohr circle against the failure line (Fig. 5). From simple geometry and employing Eqs. (11) and (12), we obtain the critical pressure increase,

$$\delta p_f = \frac{1}{2}\left(\frac{W}{L^2} + \rho' g H_0\right)\left((1+K_0) - \frac{1-K_0}{\sin(\tan^{-1}\mu_f)}\right). \tag{14}$$

Defining the frictional parameter

$$\alpha_f := (1+K_0) - \frac{1-K_0}{\sin(\tan^{-1}\mu_f)}, \tag{15}$$

and expressing in terms of a piezometric head increment, $h_f = \delta p_f/(\rho_f g)$, we arrive at the expression

$$h_f = \frac{1}{2}\frac{\frac{W}{L^2} + \rho' g H_0}{\rho_f g}\alpha_f. \tag{16}$$

In this simplified analysis, we conclude that failure leading to a conduit opening will take place if the

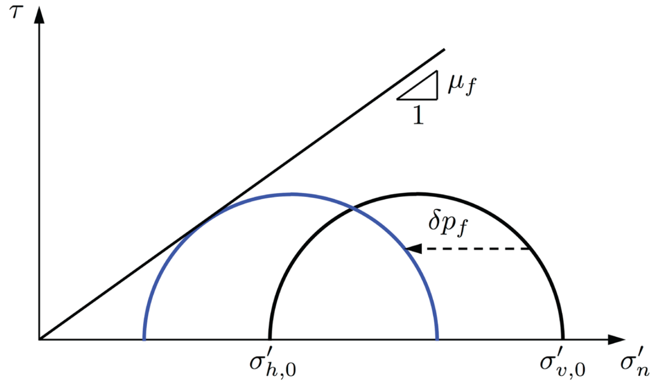

FIG. 5. Mohr-circle interpretation of the Mohr-Coulomb failure criterion [Eq. (13)]. Because the diagram is expressed in terms of effective stresses, $\sigma'_n = \sigma_n - p_f$, an increase in fluid pressure ($\delta p_f > 0$) results in a decrease in the effective normal stress $\sigma'_n$, shifting the Mohr circle to the left, towards the Mohr-Coulomb failure line.

piezometric head increase at steady state predicted by the poroelastic model at a distance $\bar{r}$ a few bead diameters away from the injection point,

$$h_{\mathrm{ss}}(\bar{r}) \equiv h(\bar{r}, t \to \infty) = \frac{2q}{4\pi K}\frac{1}{\bar{r}}\left(1 - \frac{\bar{r}}{R}\right), \tag{17}$$

is greater than the threshold failure head, $h_f$. Given that this condition is satisfied, we estimate the time of failure as the time at which $h(\bar{r}, t_f) = h_f$. Combining Eqs. (9) and (16), we arrive at the nonlinear equation for the *time of failure*, $t_f$:

$$\sum_{n=1}^{\infty} \frac{1}{1 + \frac{R-a}{a}(1 + a^2\lambda_n^2)} \frac{\sin[\lambda_n(R - \bar{r})]}{\sin[\lambda_n(R - a)]} \exp(-D\lambda_n^2 t_f) = \left(1 - \frac{\bar{r}}{R}\right) - \frac{\bar{r}}{2q/(4\pi K)} h_f. \tag{18}$$

### C. Cavity or conduit opening after frictional failure

Once the failure condition has been reached, the granular pack is mobilized. This mobilization leads to the opening of a conduit near the inlet and macroscopic deformation of the skeleton—an effect that results in displacement of the top lid to accommodate this deformation.

Given that the constituents of the porous pack (beads and fluids) are assumed to be incompressible, fluid mass conservation integrated over the entire cell dictates that

$$q(t) = q_{\mathrm{out}}(t) + L^2\dot{H}, \tag{19}$$

where $q_{\mathrm{out}}$ is the flow rate out of the cell by seepage through the porous top lid, and $\dot{H}$ is the top-lid displacement velocity. The occurrence of seepage and lid displacement poses the simple question of what the balance is between the two terms on the right-hand side of Eq. (19): (1) if $q \approx q_{\mathrm{out}}$, fluid invasion takes place by fluid displacement without cavity expansion, and (2) if $q \approx L^2\dot{H}$, fluid invasion is accommodated exclusively by cavity expansion. Therefore, Eq. (19) implicitly reflects a balance between viscous resistance and frictional resistance.

Given the fast transient of the poroelastic solution $h(r, t)$ towards steady state (Fig. 4) and that $\bar{r}$ is close to the injection port, we assume that the piezometric head is given by the steady-state solution, $h_{\mathrm{ss}}(\bar{r})$, but limited to $h_f$, i.e.,

$$h_f = h_{\mathrm{ss}}(\bar{r}) = h(\bar{r}, t \to \infty) = \frac{2q_{\mathrm{out}}}{4\pi K}\frac{1}{\bar{r}}\left(1 - \frac{\bar{r}}{R}\right). \tag{20}$$

From Eqs. (19) and (20), we obtain a nonlinear equation involving the *displacement rate* $\dot{H}$:

$$\frac{1}{L^2}\left(q - \frac{2\pi K\bar{r}}{1 - \bar{r}/R} h_f\right) = \dot{H}, \tag{21}$$

where $h_f$ is dependent on $W$ and the frictional parameter $\alpha_f$ through Eq. (16).

Qualitatively, the balance between viscous resistance and frictional resistance can be expressed as a *frictional failure number*, $N_f$, defined as the ratio of the piezometric head increase from the poroelastic solution $h_{\mathrm{ss}}$ [Eq. (17)] to the piezometric head increase for frictional failure $h_f$ [Eq. (16)]:

$$N_f \coloneqq \frac{h_{\mathrm{ss}}}{h_f}. \tag{22}$$

If $N_f \ll 1$, friction is dominant and there is no deformation. This situation is favored for a low injection rate ($q\downarrow$), a high medium permeability ($k \uparrow$), a low fluid viscosity ($\eta\downarrow$), and a high confining weight ($W \uparrow$). If $N_f \gg 1$, the opposite is true: a viscous pressure drop is dominant, causing cavity expansion.

## IV. RESULTS: MACROSCOPIC DEFORMATION

### A. Evolution of lid position

The macroscopic deformation of the granular pack is reflected in the displacement of the top lid, $H(t) - H_0$. The evolution of this quantity for a typical experiment shows that the displacement is negligible for a short period of time, and it then increases at an approximately constant rate (Fig. 6). Such behavior is congruent with our poroelastic Coulomb-failure model, in which there is an induction time in which pressure increases due to injection in a small-deformation configuration, and a frictional-sliding stage in which (constant-rate) injection leads to (constant-rate) displacement of the top lid.

### B. Model fit to failure onset and cavity expansion

We now probe whether the conceptual and mathematical model of poroelastic evolution followed by frictional failure and conduit opening is a valid representation of the

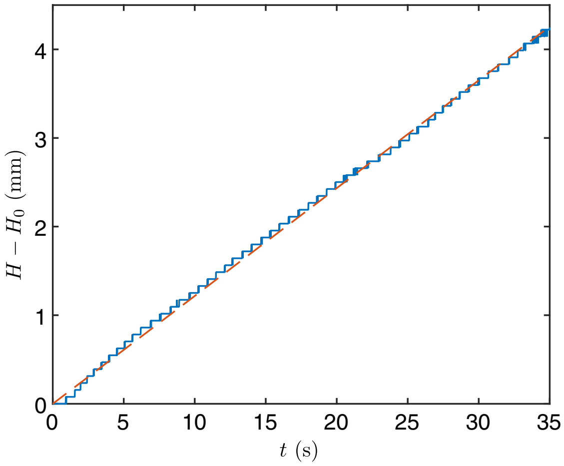

FIG. 6. Displacement of the top lid of the cell as a function of time, $H(t) - H_0$. The solid line represents the experimental data, whereas the dashed line is a linear fit. The data correspond to an experiment with $L = 6$ cm, $d = 1$ mm, $W = 18.83$ N, $H_0 = 51$ mm and $q = 45\ \mathrm{ml\,min^{-1}}$.

fluid-fluid displacement in a deformable granular pack observed in the experiments. To perform this interrogation of the data from the lens of the model, we identify the parameters that are common to all experiments and known $(\rho_f, \eta_f, \rho', g, \gamma)$, the parameters that are experiment specific and also known $(H_0, d, k, W, q)$, and the parameters that are experiment specific and *unknown*: the frictional parameter $\alpha_f$, the effective radius of granular failure $\bar{r}$, and the effective dry bulk modulus $K_d$.

To constrain these three parameters, we utilize the experimental data of lid position as a function of time binarized into two quantities for each experiment: the failure time $t_f$ and the lid displacement rate $\dot{H}$. We perform a least-squares minimization of the parameters of the model in terms of these two quantities using Eqs. (18) and (21).

Because of the scatter in the experimental measurements, it proves to be useful to perform this least-squares minimization in two steps. The first is the identification of ranges of joint pair values $(\bar{r}, \alpha_f)$ that best match the measurements of $\dot{H}$. This global minimization leads to a Pareto curve in $(\bar{r}, \alpha_f)$ space for all three experimental sets (Fig. 7).

Identification of $K_d$ from minimization of the model and the $t_f$ data [Eq. (18)], however, turns out to be challenging—likely because of the inherent uncertainty in the identification of the failure time, which results in a large range of possible values of the effective dry bulk modulus. This additional data set does allow us, however, to provide

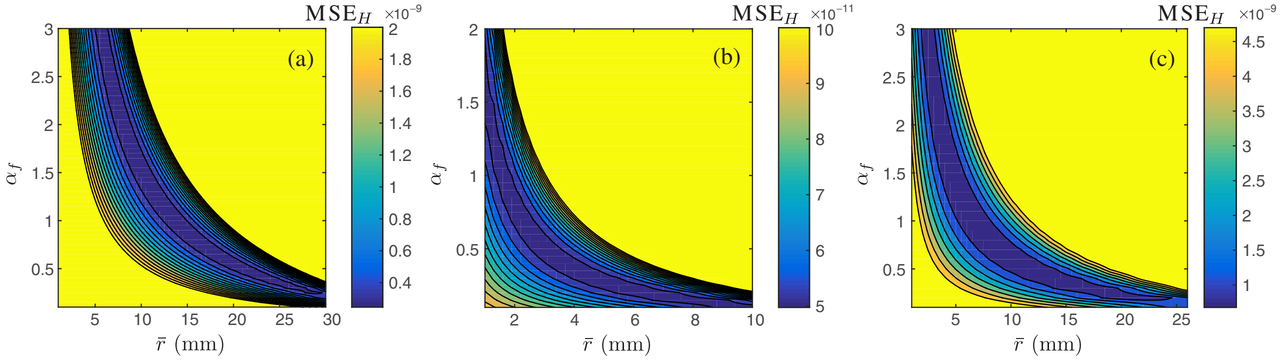

FIG. 7. Mean squared error (MSE) for $\dot{H}$ in $(\bar{r}, \alpha_f)$ space, illustrating that there is a Pareto curve that minimizes the MSE. Shown are the three sets of experimental data: (a) $L = 6$ cm, $d = 1$ mm; (b) $L = 2$ cm, $d = 1$ mm; and (c) $L = 6$ cm, $d = 3$ mm.

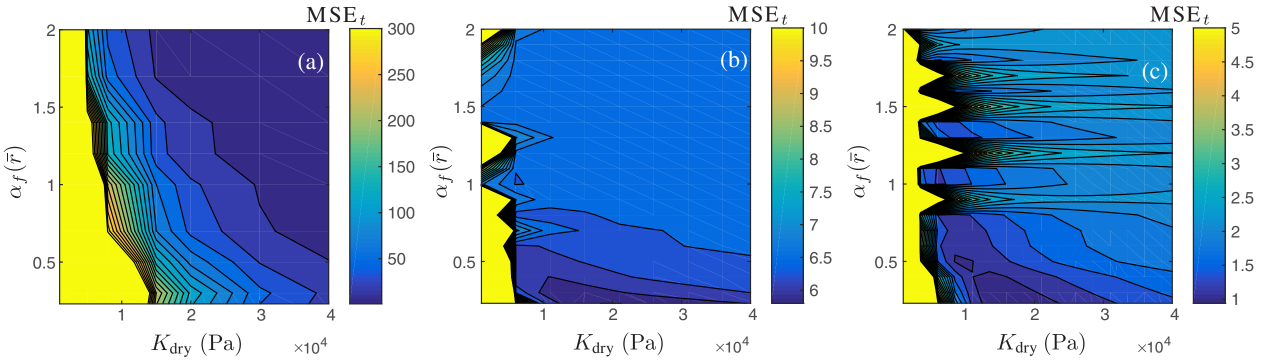

FIG. 8. Mean squared error for $t_f$ in $(K_d, \alpha_f)$ space, where the relationship $\alpha_f = \alpha_f^{\mathrm{opt}}(\bar{r})$ from the Pareto curve in Fig. 7 is already incorporated. The plots illustrate that $K_d$ is not well constrained by the data. Shown are the three sets of experimental data: (a) $L = 6$ cm, $d = 1$ mm; (b) $L = 2$ cm, $d = 1$ mm; and (c) $L = 6$ cm, $d = 3$ mm.

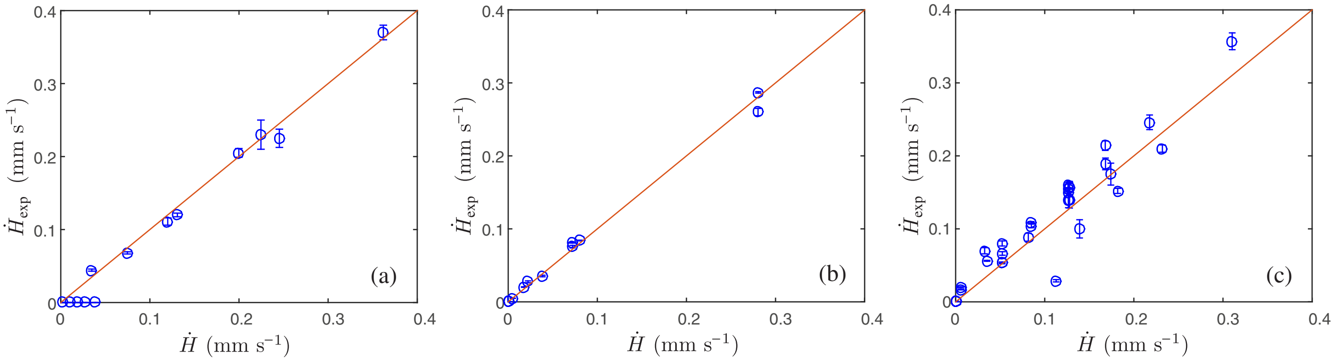

FIG. 9. Model fit for lid displacement rate $\dot{H}$ [Eq. (21)]. The red solid line indicates the 1∶1 line denoting the perfect match between theory and experiment. Shown are the three sets of experimental data: (a) $L = 6$ cm, $d = 1$ mm; (b) $L = 2$ cm, $d = 1$ mm; and (c) $L = 6$ cm, $d = 3$ mm.

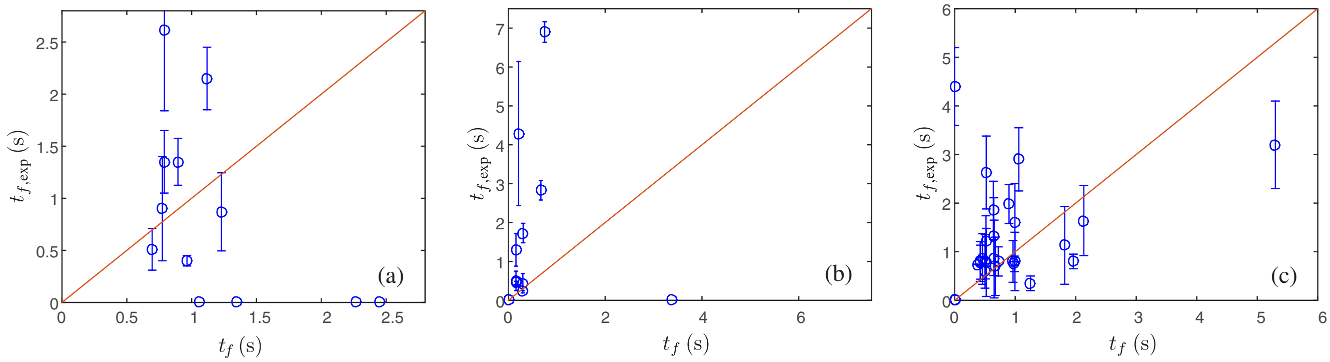

FIG. 10. Model fit for time of failure $t_f$ [Eq. (18)]. The red solid line indicates the 1∶1 line denoting the perfect match between theory and experiment. Shown are the three sets of experimental data: (a) $L = 6$ cm, $d = 1$ mm; (b) $L = 2$ cm, $d = 1$ mm; and (c) $L = 6$ cm, $d = 3$ mm.

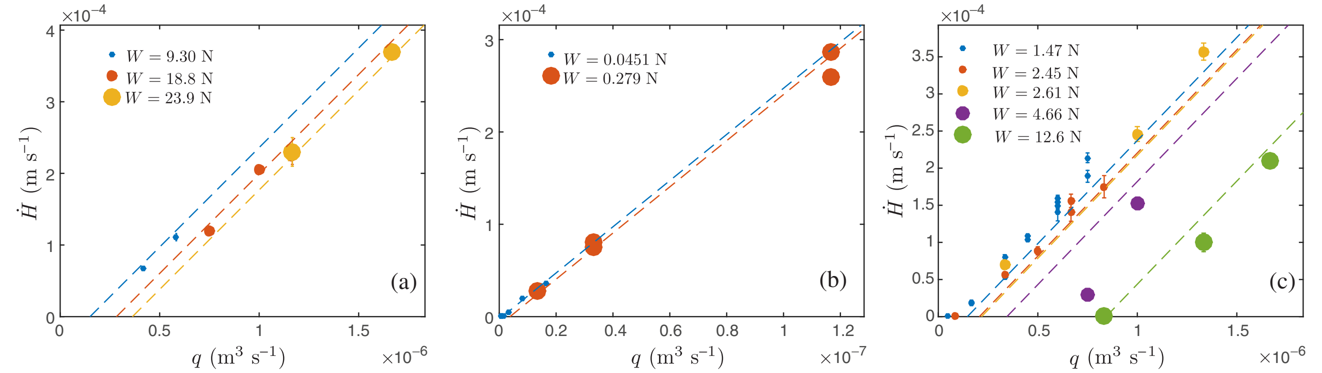

FIG. 11. Model prediction and experimental data for lid displacement rate $\dot{H}$ as a function of injection rate $q$ [Eq. (21)]. Different symbols represent different confining weights $W$. Shown are the three sets of experimental data: (a) $L = 6$ cm, $d = 1$ mm; (b) $L = 2$ cm, $d = 1$ mm; and (c) $L = 6$ cm, $d = 3$ mm.

additional constraints on the frictional parameter $\alpha_f$ (Fig. 8).

We interpret the results of the parameter fitting as follows:

(1) The frictional parameter $\alpha_f$ is a measure of the frictional resistance of the pack. It is, in principle, a material parameter dependent on the friction coefficient $\mu_f$ and the coefficient of lateral stress at rest $K_0$, and typical values for these two coefficients would render $\alpha_f \in [0, 1]$. For experiment series 2 and 3 ($L/d \approx 20$), the experimental data further suggest that a value of $\alpha_f \approx 0.5$ provides the best fit—a value that

comes naturally from taking $\mu_f \approx 0.6$ and $K_0 \approx 0.5$. For experiment series 1 ($L/d \approx 60$), the best fit occurs for a higher value, $\alpha_f \approx 1$.

(2) The effective failure distance $\bar{r}$ is on the order of 5–10 mm, or a few bead diameters, as would be expected from breaking the arches of force chains around the injection point.

(3) The effective dry bulk modulus $K_d$ remains relatively unconstrained by the data, but is on the order of 5–20 kPa, with values on the low end of this range for experiment series 2 and 3—with a lower $L/d$ value and likely looser packing due to wall effects—and on the high end of the range for experiment series 1.

The results of the model fit against the experimental values of $\dot{H}$ and $t_f$ are shown in Figs. 9 and 10, respectively. It is apparent that, while the frictional-sliding model explains postfailure deformation ($\dot{H}$) nicely, the onset of failure ($t_f$) in these granular systems is plagued with scatter, making its prediction challenging. Overall, however, the model offers a good parsimonious explanation—over a wide range of experimental conditions—of the pressurization, frictional failure, and conduit opening as a result of fluid-fluid displacement in our granular system (Fig. 11).

## V. RESULTS: PATTERNS OF FLUID INVASION AND MEDIUM DEFORMATION

To gain insight into the details of fluid-fluid displacement and the morphodynamics of deformation, we resort to 3D dynamic imaging of the granular pack at the subpore scale, using the PLIF imaging technique described in Sec. II B.

### A. Fluid invasion pattern

We first confirm that we can reconstruct the 3D dynamic fluid invasion pattern with fidelity. The process of 3D reconstruction involves thresholding the images, with a depth-dependent threshold that accounts for the inevitable finite transparency of the beads and fluids—images on a plane farther from the camera are less bright than those on a plane closer to the camera. Because of the sharp contrast between the invading fluid and the defending fluid and beads, the thresholding employed for binarizing the images is straightforward to select and does not have a significant impact on the results. The other inevitable artifact in the 3D dynamic imaging is the finite time that it takes to perform a scan (in our case, on the order of 1.2 s), and we assume that the invasion pattern does not change much during that period of time. Using the thresholded images pertaining to one full scan, we reconstruct the 3D pattern for each experiment [see Fig. 12(b) for a typical example].

To check the validity of our image analysis, we compute the volume of fluid injected $V_{\mathrm{inj}}$ by counting the voxels inside the injected pattern, and we compare this volume with the known injected volume from the pump, $q$ [Fig. 12(a)]. The good agreement between the two volumes gives us confidence that the reconstructed fluid invasion is well captured by the 3D dynamic imaging. For example, for experiments with an injection rate $q < 40\ \mathrm{ml\,min^{-1}}$, the front advances less than one bead diameter during a scan, and the assumption that the pattern does not change during one scan is valid for all practical purposes.

### B. Fractal dimension

The fractal dimension of a pattern has been employed widely to categorize dynamic processes into "universality classes" [60–64]. Most analyses of fractal dimension in fluid-fluid displacements in porous media have been restricted to 2D problems (see, e.g., Refs. [65–80]). Determination of the fractal dimension in 3D displacements has been hindered either by direct imaging, which permits only a 2D projection of the invading pattern [43], or by limited spatial and temporal resolution of the 3D scans [45]. Recent studies using PLIF imaging [46,47], confocal microscopy [48], or high-energy x-ray imaging [50,51] resolve the displacements at the pore level, but the imaged volume is insufficient to ascertain the macroscopic pattern and the fractal dimension.

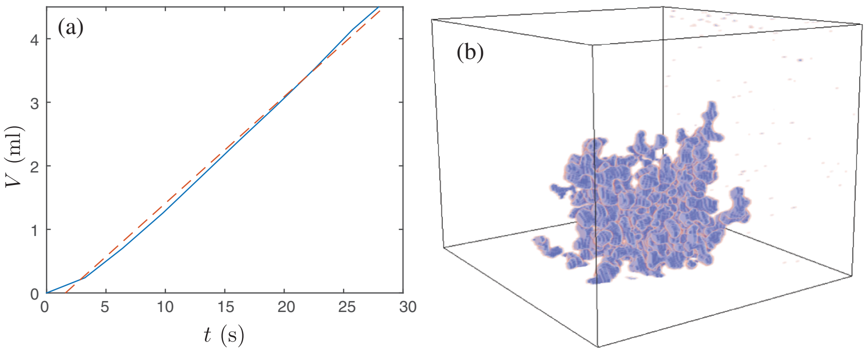

FIG. 12. Fluid invasion pattern. (a) Injected volume as a function of time. The blue solid line represents the volume reconstructed from 3D dynamic imaging; the red dashed line is a fit with an imposed slope equal to the injection rate $q$. (b) Reconstructed 3D injection pattern at $t = 16.2$ s. The base of the cube is of size $L = 6$ cm. Experiment with $q = 10\ \mathrm{ml\,min^{-1}}$, $d = 3$ mm, and $W = 1.47$ N.

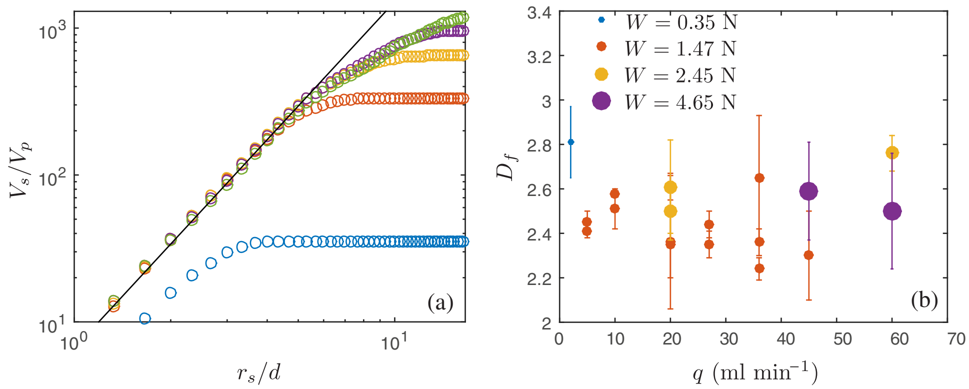

FIG. 13. Fractal dimension. (a) $V_s/V_p$ as a function of $r_s/d$, where $V_s$ is the volume of the injected liquid inside a half sphere of radius $r_s$ centered at the injection point. $V_p$ is the characteristic volume of a single pore, and $d$ is the nominal bead diameter. The different colors correspond to scans at different times $t$. The solid line represents a linear fit for $r_s < 18$ mm, which we consider to be unaffected by boundary effects and has, in this case, a slope of 2.50. The plot corresponds to an experiment with $d = 3$ mm, $L = 6$ cm, $W = 1.47$ N, and $q = 36$ ml min$^{-1}$. (b) Fractal dimension $D_f$ estimated for different experiments with a differing injection rate $q$ and confining weight $W$, with $L = 6$ cm and $d = 3$ mm.

We determine the fractal dimension from the sequence of 3D images in our experiments. For a given experiment and at a given time $t$, we compute the volume $V_s$ of injected fluid inside a semisphere centered at the injection port and of radius $r_s$. By plotting $V_s$ (rescaled by the characteristic volume $V_p$ of a single pore) as a function of $r_s$ (rescaled by the nominal bead diameter $d$), we obtain curves that display a power-law behavior that extends with time, up to the point when the morphology of the invading pattern starts to be affected by the cell boundaries [Fig. 13(a)]. We determine the fractal dimension $D_f$ of the invading pattern to be the slope of that power law, and we obtain the results shown in Fig. 13(b). The experimental data exhibit such sufficient scatter that it is difficult to observe clear trends of $D_f$ as a function of the two control variables (injection rate $q$ and confining weight $W$) for the range probed experimentally. We interpret this behavior as being the result of (1) large variability among experiments due to the relatively small volume available for sampling, and (2) the fluid-fluid displacement is affected by fingering, regardless of the presence or absence of deformation of the granular pack.

For intermediate times within each experiment, we can evaluate the capillary number directly as $\mathrm{Ca} = \eta_{\mathrm{def}} v_{\mathrm{front}}/\gamma$. For our experiments, this calculation results in values in the range $\mathrm{Ca} \in [0.03, 1]$, for which we expect viscous-dominated displacements. In this sense, the values of fractal dimension that we measure ($D_f \sim 2.5$) are consistent with the values expected from viscous fingering [43].

### C. Pore opening and conduit pattern

To confirm this hypothesis, we image simultaneously and in high resolution the invasion of the injected fluid and the deformation of the granular pack. First, we determine the position of the individual beads before the beginning of the injection of the invading fluid (Fig. 14). The bead-pack structure can be resolved throughout the experiment. At any given time $t_n$, the pattern of the injected fluid is entirely within the pore volume. At the time of the next scan, $t_{n+1}$, the injected pattern constitutes a larger volume, and a fraction of that volume may consist of regions where beads are displaced: we denote that volume of displaced solid between scans as the "conduit volume."

In Fig. 15, we show 3D renderings of the injection pattern (in white) and the conduit volume (in red) for experiments corresponding to $L = 6$ cm, $d = 3$ mm, and $W = 1.47$ N, and differing injection rates $q$. It is apparent that, as the injection rate increases, the amount of bead displacement also increases, from virtually no bead displacement at the lowest value of $q$ [Fig. 15(a)] to a conduit volume fraction of about 45% for $q = 40$ ml min$^{-1}$ [Fig. 15(f)]. The numeric values of this trend between the conduit volume fraction and the injection rate are shown in Fig. 16.

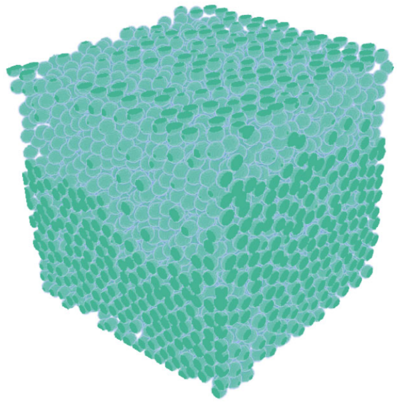

FIG. 14. Position of the glass beads at the beginning of fluid injection. Experiment with $L = 6$ cm and $d = 3$ mm.

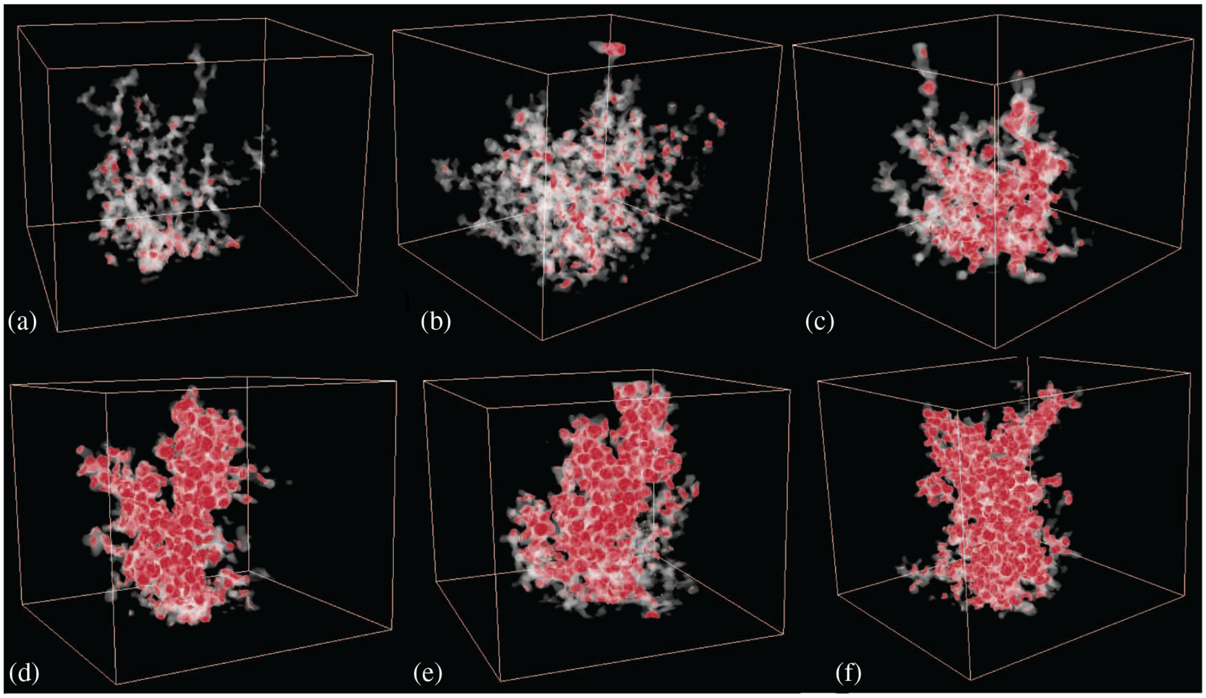

FIG. 15. Injection pattern (in white) superimposed on the conduit volume (in red) near the time of breakthrough for experiments with $L = 6$ cm, $d = 3$ mm, and $W = 1.47$ N. (a) $q = 2$ ml min$^{-1}$ at $t = 108$ s and $V = 2.1$ ml. (b) $q = 5$ ml min$^{-1}$ at $t = 61$ s and $V = 4.7$ ml. (c) $q = 10$ ml min$^{-1}$ at $t = 29$ s and $V = 4.7$ ml. (d) $q = 20$ ml min$^{-1}$ at $t = 12.8$ s and $V = 3.8$ ml. (e) $q = 27$ ml min$^{-1}$ at $t = 9.6$ s and $V = 3.6$ ml. (f) $q = 36$ ml min$^{-1}$ at $t = 12.7$ s and $V = 6.8$ ml.

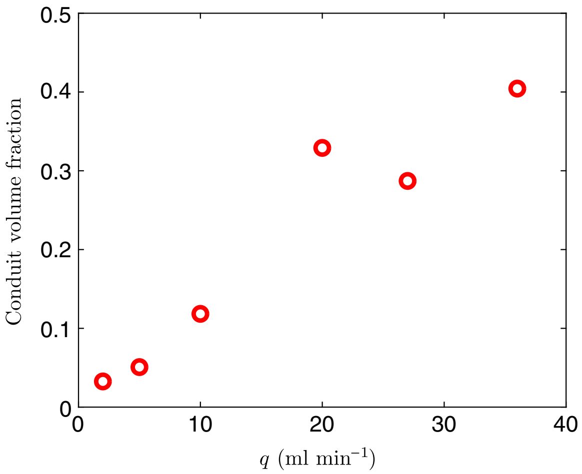

FIG. 16. Fraction of the fluid invasion volume that corresponds to the volume involving bead displacement, for different injection rates $q$.

This direct pore-scale observation is consistent with the macroscopic measurements of lid displacement, and it is compatible with our model of frictional failure.

## VI. CONCLUSIONS

In this work, we elucidate the role of grain displacement in the evolution of injection patterns in granular media by means of direct 3D observations of the dynamic process at the pore scale. We reconcile observations of fluid invasion morphology with the underlying pore-scale physics. We find that the onset and evolution of macroscopic displacement can be captured with a simple model of frictional failure.

Our results open the door to a better understanding, quantification, and eventual prediction of processes in which the poromechanics of multiphase mixtures plays a central role, such as soil desiccation [16,39], magma degassing [15], methane venting from sediments [11,14,42], and hydraulic fracturing of hydrocarbon formations [81]. Our 3D PLIF experimental setup is also allowing us to study other multiphase porous-media processes such as buoyancy-driven fingering, an instability that controls rainwater infiltration in soils (see, e.g., Refs. [6,7,82]) and hydrocarbon migration in sedimentary basins (see, e.g., Refs. [49,75,83]).

We plan to extend our investigation in a number of directions. For example, we are currently exploring ways to alter the wettability of the system [84–88] to investigate the impact of wettability on the emergence and morphology of conduits—the technical challenge being to maintain index matching among the two fluids and the beads. We are also conducting experiments where we measure the injection pressure to discern whether the pressure signature associated with pore-invasion events (see, e.g., Refs. [73,89–92]) is different from that of conduit opening.

## ACKNOWLEDGMENTS

We thank Luis Cueto-Felgueroso for conducting 3D finite element simulations to confirm the validity of some of the approximations in the analytical model. This work was funded in part by the U.S. Department of Energy (Grant No. DE-SC0018357). M.-J. D. acknowledges the funding provided by Eni through the Society of Energy Fellows at MIT.

[1] F. M. Orr, Jr. and J. J. Taber, Use of carbon dioxide in enhanced oil recovery, Science **224**, 563 (1984).

[2] L. W. Lake, *Enhanced Oil Recovery* (Prentice-Hall, Englewood Cliffs, NJ, 1989).

[3] D. W. Brown, D. V. Duchane, G. Heiken, and V. T. Hriscu, *Mining the Earth's Heat: Hot Dry Rock Geothermal Energy* (Springer, New York, 2012).

[4] Intergovernmental Panel on Climate Change, *Carbon Dioxide Capture and Storage: Special Report of the Intergovernmental Panel on Climate Change*, edited by B. Metz *et al.* (Cambridge University Press, Cambridge, England, 2005).

[5] M. L. Szulczewski, C. W. MacMinn, H. J. Herzog, and R. Juanes, Lifetime of carbon capture and storage as a climate-change mitigation technology, Proc. Natl. Acad. Sci. U.S.A. **109**, 5185 (2012).

[6] L. Cueto-Felgueroso and R. Juanes, Nonlocal Interface Dynamics and Pattern Formation in Gravity-Driven Unsaturated Flow through Porous Media, Phys. Rev. Lett. **101**, 244504 (2008).

[7] Y. Wei, C. M. Cejas, R. Barrois, R. Dreyfus, and D. J. Durian, Morphology of Rain Water Channeling in Systematically Varied Model Sandy Soils, Phys. Rev. Applied **2**, 044004 (2014).

[8] C. Y. Wang, Fundamental models for fuel cell engineering, Chem. Rev. **104**, 4727 (2004).

[9] T. Patzek, F. Male, and M. Marder, Gas production in the Barnett Shale obeys a simple scaling theory, Proc. Natl. Acad. Sci. U.S.A. **110**, 19731 (2013).

[10] L. Cueto-Felgueroso and R. Juanes, Forecasting long-term gas production from shale, Proc. Natl. Acad. Sci. U.S.A. **110**, 19660 (2013).

[11] B. P. Scandella, L. Pillsbury, T. Weber, C. Ruppel, H. Hemond, and R. Juanes, Ephemerality of discrete methane vents in lake sediments, Geophys. Res. Lett. **43**, 4374 (2016).

[12] R. Sassen, S. L. Losh, L. Cathles III, H. H. Roberts, J. K. Whelan, A. V. Milkov, S. T. Sweet, and D. A. DeFreitas, Massive vein-filling gas hydrate: Relation to ongoing gas migration from the deep subsurface in the Gulf of Mexico, Mar. Pet. Geol. **18**, 551 (2001).

[13] L.-T. Chen, N. Li, C.-Y. Sun, G.-J. Chen, C. A. Koh, and B.-J. Sun, Hydrate formation in sediments from free gas using a one-dimensional visual simulator, Fuel **197**, 298 (2017).

[14] K. Andreassen, A. Hubbard, M. Winsborrow, H. Patton, S. Vadakkepuliyambatta, A. Plaza-Faverola, E. Gudlaugsson, P. Serov, A. Deryabin, R. Mattingsdal *et al.*, Massive blow-out craters formed by hydrate-controlled methane expulsion from the arctic seafloor, Science **356**, 948 (2017).

[15] A. Parmigiani, S. Faroughi, C. Huber, O. Bachmann, and Y. Su, Bubble accumulation and its role in the evolution of magma reservoirs in the upper crust, Nature (London) **532**, 492 (2016).

[16] A. Groisman and E. Kaplan, An experimental study of cracking induced by desiccation, Europhys. Lett. **25**, 415 (1994).

[17] J. W. Peterson, P. A. Lepczyk, and K. L. Lake, Effect of sediment size on area of influence during groundwater remediation by air sparging: A laboratory approach, Environ. Geol. **38**, 1 (1999).

[18] J. S. Selker, M. Niemet, N. G. McDuffie, S. M. Gorelick, and J.-Y. Parlange, The local geometry of gas injection into saturated homogeneous porous media, Transp. Porous Media **68**, 107 (2007).

[19] N. Chakrapani, B. Wei, A. Carrillo, P. M. Ajayan, and R. S. Kane, Capillarity-driven assembly of two-dimensional cellular carbon nanotube foams, Proc. Natl. Acad. Sci. U.S.A. **101**, 4009 (2004).

[20] H. Van Damme, F. Obrecht, P. Levitz, L. Gatineau, and C. Laroche, Fractal viscous fingering in clay slurries, Nature (London) **320**, 731 (1986).

[21] E. Lemaire, P. Levitz, G. Daccord, and H. Van Damme, From Viscous Fingering to Viscoelastic Fracturing in Colloidal Fluids, Phys. Rev. Lett. **67**, 2009 (1991).

[22] C. W. MacMinn, E. R. Dufresne, and J. S. Wettlaufer, Fluid-Driven Deformation of a Soft Granular Material, Phys. Rev. X **5**, 011020 (2015).

[23] D. Vella, P. Aussillous, and L. Mahadevan, Elasticity of an interfacial particle raft, Europhys. Lett. **68**, 212 (2004).

[24] C. Peco, W. Chen, Y. Liu, J. Dolbow, M. Bandi, and E. Fried, Influence of surface tension in the surfactant-driven fracture of closely-packed particulate monolayers, Soft Matter **13**, 5832 (2017).

[25] E. R. Dufresne, E. I. Corwin, N. A. Greenblatt, J. Ashmore, D. Y. Wang, A. D. Dinsmore, J. X. Cheng, X. S. Xie, J. W. Hutchinson, and D. A. Weitz, Flow and Fracture in Drying Nanoparticle Suspensions, Phys. Rev. Lett. **91**, 224501 (2003).

[26] L. Goehring, W. J. Clegg, and A. F. Routh, Plasticity and Fracture in Drying Colloidal Films, Phys. Rev. Lett. **110**, 024301 (2013).

[27] C. Chevalier, A. Lindner, M. Leroux, and E. Clement, The instability of slow, immiscible, viscous liquid-liquid displacements in permeable media, J. Non-Newtonian Fluid Mech. **158**, 63 (2009).

[28] B. Sandnes, H. A. Knudsen, K. J. Måløy, and E. G. Flekkøy, Labyrinth Patterns in Confined Granular-Fluid Systems, Phys. Rev. Lett. **99**, 038001 (2007).

[29] B. Sandnes, E. G. Flekkøy, H. A. Knudsen, K. J. Måløy, and H. See, Patterns and flow in frictional fluid dynamics, Nat. Commun. **2**, 288 (2011).

[30] R. Holtzman, M. L. Szulczewski, and R. Juanes, Capillary Fracturing in Granular Media, Phys. Rev. Lett. **108**, 264504 (2012).

[31] R. Holtzman and R. Juanes, Crossover from fingering to fracturing in deformable disordered media, Phys. Rev. E **82**, 046305 (2010).

[32] A. K. Jain and R. Juanes, Preferential mode of gas invasion in sediments: Grain-scale mechanistic model of coupled multiphase fluid flow and sediment mechanics, J. Geophys. Res. **114**, B08101 (2009).

[33] X.-Z. Kong, W. Kinzelbach, and F. Stauffer, Morphodynamics during air injection into water-saturated movable spherical granulates, Chem. Eng. Sci. **65**, 4652 (2010).

[34] G. Varas, V. Vidal, and J.-C. Géminard, Morphology of air invasion in an immersed granular layer, Phys. Rev. E **83**, 061302 (2011).

[35] G. Varas, V. Vidal, and J.-C. Géminard, Venting dynamics of an immersed granular layer, Phys. Rev. E **83**, 011302 (2011).

[36] F. K. Eriksen, R. Toussaint, K.-J. Måløy, and E. G. Flekkøy, Invasion patterns during two-phase flow in deformable porous media, Front. Phys. **3**, 81 (2015).

[37] J.-H. Choi, Y. Seol, R. Boswell, and R. Juanes, X-ray computed-tomography imaging of gas migration in water-saturated sediments: From capillary invasion to conduit opening, Geophys. Res. Lett. **38**, L17310 (2011).

[38] H. Huang, F. Zhang, P. Callahan, and J. Ayoub, Granular Fingering in Fluid Injection into Dense Granular Media in a Hele-Shaw Cell, Phys. Rev. Lett. **108**, 258001 (2012).

[39] H. Shin and J. C. Santamarina, Fluid-driven fractures in uncemented sediments: Underlying particle-level processes, Earth Planet. Sci. Lett. **299**, 180 (2010).

[40] A. Islam, S. Chevalier, I. Ben Salem, Y. Bernabe, R. Juanes, and M. Sassi, Characterization of the crossover from capillary invasion to viscous fingering to fracturing during drainage in a vertical 2D porous medium, Int. J. Multiphase Flow **58**, 279 (2014).

[41] B. P. Boudreau, C. Algar, B. D. Johnson, I. Croudace, A. Reed, Y. Furukawa, K. M. Dorgan, P. A. Jumars, and A. S. Grader, Bubble growth and rise in soft sediments, Geology **33**, 517 (2005).

[42] B. P. Scandella, K. Delwiche, H. Hemond, and R. Juanes, Persistence of bubble outlets in soft, methane-generating sediments, J. Geophys. Res. **122**, 1298 (2017).

[43] V. Frette, J. Feder, T. Jøssang, P. Meakin, and K. J. Måløy, Fast, immiscible fluid-fluid displacement in three-dimensional porous media at finite viscosity contrast, Phys. Rev. E **50**, 2881 (1994).

[44] M. Stöhr, K. Roth, and B. Jähne, Measurement of 3D pore-scale flow in index-matched porous media, Exp. Fluids **35**, 159 (2003).

[45] H. Ovdat and B. Berkowitz, Pore-scale study of drainage displacement under combined capillary and gravity effects in index-matched porous media, Water Resour. Res. **42**, W06411 (2006).

[46] X.-Z. Kong, M. Holzner, F. Stauffer, and W. Kinzelbach, Time-resolved 3D visualization of air injection in a liquid-saturated refractive-index-matched porous medium, Exp. Fluids **50**, 1659 (2011).

[47] P. Sharma, P. Aswathi, A. Sane, S. Ghosh, and S. Bhattacharya, Three-dimensional real-time imaging of biphasic flow through porous media, Rev. Sci. Instrum. **82**, 113704 (2011).

[48] A. T. Krummel, S. S. Datta, S. Münster, and D. A. Weitz, Visualizing multiphase flow and trapped fluid configurations in a model three-dimensional porous medium, AIChE J. **59**, 1022 (2013).

[49] J. Yan, X. Luo, W. Wang, R. Toussaint, J. Schmittbuhl, G. Vasseur, F. Chen, A. Yu, and L. Zhang, An experimental study of secondary oil migration in a three-dimensional tilted porous medium, AAPG Bull. **96**, 773 (2012).

[50] S. Berg, H. Ott, S. A. Klapp, A. Schwing, R. Neiteler, N. Brussee, A. Makurat, L. Leu, F. Enzmann, J.-O. Schwarz, M. Kersten, S. Irvine, and M. Stampanoni, Real-time 3D imaging of Haines jumps in porous media flow, Proc. Natl. Acad. Sci. U.S.A. **110**, 3755 (2013).

[51] K. Singh, H. Scholl, M. Brinkmann, M. Di Michiel, M. Scheel, S. Herminghaus, and R. Seemann, The role of local instabilities in fluid invasion into permeable media, Sci. Rep. **7**, 444 (2017).

[52] J. Bear, *Dynamics of Fluids in Porous Media* (Elsevier, New York, 1972).

[53] M. A. Biot, General theory of three-dimensional consolidation, J. Appl. Phys. **12**, 155 (1941).

[54] J. Geertsma, The effect of fluid pressure decline on volumetric change of porous rocks, Trans. AIME **210**, 331 (1957).

[55] J. R. Rice and M. P. Cleary, Some basic stress-diffusion solutions for fluid saturated elastic porous media with compressible constituents, Rev. Geophys. **14**, 227 (1976).

[56] O. Coussy, *Poromechanics* (John Wiley & Sons, Chichester, England, 2004).

[57] J. Crank, *Mathematics of Diffusion*, 2nd ed. (Oxford University Press, New York, 1975).

[58] H. S. Carslaw and J. C. Jaeger, *Conduction of Heat in Solids*, 2nd ed. (Oxford University Press, New York, 1959).

[59] The IBVP given by Eqs. (5)–(8) is considered in Sec. 9.9 of Ref. [58]. Unfortunately, the expression given for the solution is demonstrably incorrect: $h(r,t)$ should initially be zero for all values of $r$ (it does not in their expression) and should increase with $t$ (which it also does not).

[60] B. B. Mandelbrot, *The Fractal Geometry of Nature* (W.H. Freeman and Co., New York, 1982).

[61] M. Kardar, G. Parisi, and Y.-C. Zhang, Dynamic Scaling of Growing Interfaces, Phys. Rev. Lett. **56**, 889 (1986).

[62] V. K. Horvath, F. Family, and T. Vicsek, Dynamic scaling of the interface in two-phase viscous flows in porous media, J. Phys. A **24**, L25 (1991).

[63] A. L. Barabási and H. E. Stanley, *Fractal Concepts in Surface Growth* (Cambridge University Press, Cambridge, England, 1995).

[64] T. Halpin-Healy and Y.-C. Zhang, Kinetic roughening phenomena, stochastic growth, directed polymers and all that. Aspects of multidisciplinary statistical mechanics, Phys. Rep. **254**, 215 (1995).

[65] L. Paterson, Diffusion-Limited Aggregation and Two-Fluid Displacements in Porous Media, Phys. Rev. Lett. **52**, 1621 (1984).

[66] K. J. Måløy, J. Feder, and T. Jøssang, Viscous Fingering Fractals in Porous Media, Phys. Rev. Lett. **55**, 2688 (1985).

[67] R. Lenormand and C. Zarcone, Invasion Percolation in an Etched Network: Measurement of a Fractal Dimension, Phys. Rev. Lett. **54**, 2226 (1985).

[68] J. Nittmann, G. Daccord, and H. E. Stanley, Fractal growth of viscous fingers: Quantitative characterization of

a fluid instability phenomenon, Nature (London) **314**, 141 (1985).

[69] G. Daccord, J. Nittmann, and H. E. Stanley, Radial Viscous Fingers and Diffusion-Limited Aggregation: Fractal Dimension and Growth Sites, Phys. Rev. Lett. **56**, 336 (1986).

[70] R. Lenormand, E. Touboul, and C. Zarcone, Numerical models and experiments on immiscible displacements in porous media, J. Fluid Mech. **189**, 165 (1988).

[71] M. A. Rubio, C. A. Edwards, A. Dougherty, and J. P. Gollub, Self-Affine Fractal Interfaces from Immiscible Displacement in Porous Media, Phys. Rev. Lett. **63**, 1685 (1989).

[72] J. F. Fernández, R. Rangel, and J. Rivero, Crossover Length from Invasion Percolation to Diffusion-Limited Aggregation in Porous Media, Phys. Rev. Lett. **67**, 2958 (1991).

[73] K. J. Måløy, L. Furuberg, J. Feder, and T. Jøssang, Dynamics of Slow Drainage in Porous Media, Phys. Rev. Lett. **68**, 2161 (1992).

[74] S. V. Buldyrev, A.-L. Barabási, F. Caserta, S. Havlin, H. E. Stanley, and T. Vicsek, Anomalous interface roughening in porous media: Experiment and model, Phys. Rev. A **45**, R8313 (1992).

[75] V. Frette, J. Feder, T. Jøssang, and P. Meakin, Buoyancy-Driven Fluid Migration in Porous Media, Phys. Rev. Lett. **68**, 3164 (1992).

[76] Y. Méheust, G. Løvoll, K. J. Måløy, and J. Schmittbuhl, Interface scaling in a two-dimensional porous medium under combined viscous, gravity, and capillary effects, Phys. Rev. E **66**, 051603 (2002).

[77] G. Løvoll, Y. Méheust, R. Toussaint, J. Schmittbuhl, and K. J. Måløy, Growth activity during fingering in a porous Hele-Shaw cell, Phys. Rev. E **70**, 026301 (2004).

[78] M. Ferer, C. Ji, G. S. Bromhal, J. Cook, G. Ahmadi, and D. H. Smith, Crossover from capillary fingering to viscous fingering for immiscible unstable flow: Experiment and modeling, Phys. Rev. E **70**, 016303 (2004).

[79] R. Toussaint, G. Løvoll, Y. Méheust, K. J. Måløy, and J. Schmittbuhl, Influence of pore-scale disorder on viscous fingering during drainage, Europhys. Lett. **71**, 583 (2005).

[80] K. A. Takeuchi, M. Sano, T. Sasamoto, and H. Spohn, Growing interfaces uncover universal fluctuations behind scale invariance, Sci. Rep. **1**, 34 (2011).

[81] M. K. Hubbert and D. G. Willis, Mechanics of hydraulic fracturing, Petrol. Trans. AIME **210**, 153 (1957).

[82] H. Gomez, L. Cueto-Felgueroso, and R. Juanes, Three-dimensional simulation of unstable gravity-driven infiltration of water into a porous medium, J. Comput. Phys. **238**, 217 (2013).

[83] P. Meakin, G. Wagner, A. Vedvik, H. Amundsen, J. Feder, and T. Jøssang, Invasion percolation and secondary migration: Experiments and simulations, Mar. Pet. Geol. **17**, 777 (2000).

[84] J. P. Stokes, D. A. Weitz, J. P. Gollub, A. Dougherty, M. O. Robbins, P. M. Chaikin, and H. M. Lindsay, Interfacial Stability of Immiscible Displacement in a Porous Medium, Phys. Rev. Lett. **57**, 1718 (1986).

[85] D. A. Weitz, J. P. Stokes, R. C. Ball, and A. P. Kushnick, Dynamic Capillary Pressure in Porous Media: Origin of the Viscous-Fingering Length Scale, Phys. Rev. Lett. **59**, 2967 (1987).

[86] B. Levaché and D. Bartolo, Revisiting the Saffman-Taylor Experiment: Imbibition Patterns and Liquid-Entrainment Transitions, Phys. Rev. Lett. **113**, 044501 (2014).

[87] M. Trojer, M. L. Szulczewski, and R. Juanes, Stabilizing Fluid-Fluid Displacements in Porous Media through Wettability Alteration, Phys. Rev. Applied **3**, 054008 (2015).

[88] B. Zhao, C. W. MacMinn, and R. Juanes, Wettability control on multiphase flow in patterned microfluidics, Proc. Natl. Acad. Sci. U.S.A. **113**, 10251 (2016).

[89] L. Furuberg, K. J. Måløy, and J. Feder, Intermittent behavior in slow drainage, Phys. Rev. E **53**, 966 (1996).

[90] M. Jankov, G. Løvoll, H. A. Knudsen, K. J. Måløy, R. Planet, and R. Toussaint, Effects of pressure oscillations on drainage in an elastic porous medium, Transp. Porous Media **84**, 569 (2010).

[91] F. Moebius and D. Or, Interfacial jumps and pressure bursts during fluid displacement in interacting irregular capillaries, J. Colloid Interface Sci. **377**, 406 (2012).

[92] F. Moebius and D. Or, Pore scale dynamics underlying the motion of drainage fronts in porous media, Water Resour. Res. **50**, 8441 (2014).